Journal of Physics D: Applied Physics

PAPER

Controlled growth of silicon particles via plasma pulsing and their application as battery material

To cite this article: Joseph Schwan *et al* 2022 *J. Phys. D: Appl. Phys.* **55** 094002

IOP Publishing
Journal of Physics D: Applied Physics
J. Phys. D: Appl. Phys. **55** (2022) 094002 (11pp)
https://doi.org/10.1088/1361-6463/ac3867

Controlled growth of silicon particles via plasma pulsing and their application as battery material

Joseph Schwan[1], **Brandon Wagner**[2], **Minseok Kim**[1] and **Lorenzo Mangolini**[1,2,*]

[1] Mechanical Engineering Department, University of California Riverside, Riverside, CA 92521,
United States of America
[2] Materials Science and Engineering Program, University of California Riverside, Riverside, CA 92521,
United States of America

E-mail: lmangolini@engr.ucr.edu

Received 21 August 2021, revised 3 November 2021
Accepted for publication 10 November 2021
Published 23 November 2021

Abstract

The use of silicon nanoparticles for lithium-ion batteries requires a precise control over both their average size and their size distribution. Particles larger than the generally accepted critical size of 150 nm fail during lithiation because of excessive swelling, while very small particles (<10 nm) inevitably lead to a poor first cycle coulombic efficiency because of their excessive specific surface area. Both mechanisms induce irreversible capacity losses and are detrimental to the anode functionality. In this manuscript we describe a novel approach for enhanced growth of nanoparticles to ∼20 nm using low-temperature flow-through plasma reactors via pulsing. Pulsing of the RF power leads to a significant increase in the average particle size, all while maintaining the particles well below the critical size for stable operation in a lithium-ion battery anode. A zero-dimensional aerosol plasma model is developed to provide insights into the dynamics of particle agglomeration and growth in the pulsed plasma reactor. The accelerated growth correlates with the shape of the particle size distribution in the afterglow, which is in turn controlled by parameters such as metastable density, gas and electron temperature. The accelerated agglomeration in each afterglow phase is followed by rapid sintering of the agglomerates into single-crystal particles in the following plasma-on phase. This study highlights the potential of non-thermal plasma reactors for the synthesis of functional nanomaterials, while also underscoring the need for better characterization of their fundamental parameters in transient regimes.

Keywords: pulsed operation, silicon anode, plasma aerosol

(Some figures may appear in color only in the online journal)

1. Introduction

Flow-through low-temperature plasma reactors provide a simple and effective approach for the synthesis of nanoscale silicon particles [1, 2]. These reactors can rapidly consume the chemical precursors such as silane gas and convert it into sub-10 nm unagglomerated particles. The capability of producing small particles with a narrow size range makes this process particularly interesting for the synthesis of next-generation battery materials. Silicon has received considerable attention in this area, because of its high lithiation capacity [3–6]. Still, this application is sensitive to the size distribution of the utilized silicon particles, as our group has recently shown by comparing the performance of commercial silicon particles of nominally the same size [7]. Particles in the large size tail of the distribution, with diameters above the generally accepted critical size of ∼150 nm [8], are more likely to

---

[*] Author to whom any correspondence should be addressed.

fail during repeated lithiation–delithiation cycles. Even though commercial silicon samples may have a small fraction of particles above the critical size, these particles occupy a significant volume fraction of the overall sample. Their mechanical failure due to swelling upon lithiation induces significant loss in anode capacity. It would be highly desirable to have access to silicon particles with a narrow size distribution, without particles at or above the critical size range. On the other hand, the reduction in particle size and the corresponding increase in specific surface area has drawbacks in terms of low 1st cycle Coulombic efficiency. This is a consequence of electrolyte decomposition at the surface of the active material during the first charging cycles, which results in an irreversible loss of lithium to form a shell known as the solid electrolyte interphase (SEI). This is highly detrimental for the battery stability, particularly when the anode is interfaced with a real-life cathode material (like lithium iron phosphate or lithium nickel manganese cobalt oxide), as opposed to the lithium metal which is broadly used by the scientific community, but that is not compatible with commercial applications.

These considerations motivate this investigation, which aims at producing silicon powders with a narrow size distribution, but in sizes that are larger than the sub-10 nm particles typically produced by low-temperature plasma reactors. We have found that by operating the radio frequency-driven plasma in a square wave ‘pulsed mode’ it is possible to significanlty increase the average nanoparticle size, from $\sim$8 nm for the case of a continuous plasma to $\sim$20 nm for a pulsed plasma, all while maintaining a fairly narrow size distribution and with no particles above 100 nm in size. We have verified the electrochemical performance of the material and found that the particles produced via the pulsed-plasma indeed show significantly larger 1st cycle Coulombic efficiency compared to the continuous plasma case.

Our choice of exploring pulsed operation as a mean to tune the particle size is motivated by recent reports discussing the particle charge dynamics in spatial afterglows, i.e. immediately downstream of the plasma volume [9, 10], confirming that the particle charge relaxes in the afterglow and can even become positive depending on process condition, leading to an electrostatically-enhanced agglomeration rate. The complex plasma and dust dynamics in afterglows have attracted the interest of several groups, with the majority of these investigations being of a theoretical nature [11–16]. With this work, we explore the use of pulsed plasma operation to leverage the enhanced particle agglomeration rate in the afterglow, provide an additional mean to tune particle size, and ultimately realize materials with improved functionality for applications in energy storage.

Given the potential of plasma pulsing for improving material functionality, we have developed a zero-dimensional plasma aerosol model to both investigate the dynamics of particle charge relaxation in the afterglow and to provide a tool that can aid in the choice of process parameters, thus enabling further improvements in the material functionality. Results from this model show good qualitative agreement with the experimental observation in term of particle growth rate, confirming that the systems switches from a configuration in which electrostatic effects slow down agglomeration while the plasma is on, to a configuration in which electrostatic effects actually increase the particle agglomeration rate in the afterglow because of the presence of both negatively and positively charged particles. Still, our model predict a smaller degree of particle growth in the afterglow compared to the experimental observation. This underscores the need for better characterization of these systems in terms of parameters, such as argon metastable density, gas temperature, and kinetics of electron cooling in the afterglow. We have found that all of these parameters affect the particle charge distribution in the afterglow, which in turn affects the kinetics of particle growth via coagulation.

2. Experimental details

This silicon synthesis system consists of a 2.54 cm (1′) diameter quartz tube fed with a precursor of 1.37% silane (SiH_4)-argon mixture at a 100 standard cubic centimeters per minute (sccm) volume flow rate. SiH_4 is a common precursor for this type of processes, and low-temperature plasmas rapidly initiate the particle nucleation process in silane-containing mixtures [17]. In addition, the cost of anode materials amounts to only a small fraction of the total battery cost, alleviating concerns related to the cost of silane as precursor for silicon nanoparticle synthesis [18]. The precursor gas is excited into a nonthermal plasma state within the quartz tube through the use of a 13.56 MHz electrical signal supplied by a 2.54 cm thick copper ring electrode. The electrode is wrapped around the outside of the reactor chamber and placed equidistant from the grounded metal flanges on each end of the reactor so as to fill the entire chamber volume with plasma. This setup corresponds to a capacitively coupled plasma, with the RF-biased electrode coupling to the grounded flanges. The flow rate is maintained by an MKS 1179C mass flow controller, while the electrode is powered by an RFPP RF-5S Advanced Energy power supply matched to the reactor’s electrical impedance using an MFJ-989D matching network. Both constant and pulsed plasmas are supplied with 100 W of power, with both high time and duty cycle controlled through the power supply. Reactor pressure is controlled through the use of an MKS digital/analogue pressure control system with a capacitive pressure gauge. The reactor is evacuated with a roughing pump to a base pressure of $\sim$1 Pa. The leakage rate is tested before each nanoparticle production run, which does not proceed unless the leakage rate is as low as $\sim$2.5 Pa min^{-1} or less. Moreover, a cleaning plasma in an argon-hydrogen mixture is ignited before any production run to remove any contaminants potentially absorbed onto the reactor walls. Synthesized material is caught on 5 μm stainless steel mesh, held downstream of the reactor at a sufficient distance to avoid any coupling between the plasma and the collection mesh. Vacuum is maintained by an Edwards 28 E2M28 rotary vane pump.

The average diameter of the pure silicon material is analyzed through Scherrer’s analysis performed on x-ray diffraction (XRD) spectra collected on a PANalytical Empyrean Series 2. Transmission electron microscopy (TEM) is carried out on a Tecnai T12 to verify the size predicted by the XRD data and to gather size distributions through direct measurement of imaged particles. These TEM grids are prepared by temporarily directing the reactor output through the TEM grid while under vacuum conditions.

For the experiments discussed in this manuscript, the reactor length is 10.1 cm. This gives a residence, based on the flow velocity, of 100 ms for a flow rate of 100 sccm, at a pressure of 526 Pa (4 Torr).

The system has been characterized over a wide range of pressures, varying from ∼65 Pa to ∼4200 Pa (0.5 Torr and 32 Torr). The effect of pulsing has been investigated at 131.5, 263, 526 and 1052 Pa (1, 2, 4 and 8 Torr) with a minimum plasma-on time of 2 ms (corresponding to a frequency of 250 Hz) as limited by the capability of our RF power supply.

For successful cycling of silicon in a lithium-ion (Li-ion) half-cell, a conductive matrix of non-reactive carbon is generally used. Recent advances in chemical vapor deposition (CVD) particle coating techniques have allowed for the controlled deposition of conformal graphitic carbon shells around each particle [6]. After silicon synthesis, the pure silicon material is collected and exposed to 40 sccm of acetylene at a pressure of 50 000 Pa and at a temperature of 650 °C for 30 min to achieve carbon coating, then placed under 20 sccm of argon at 1000 °C at 263 Pa (2 Torr) for 10 min to promote the carbon shell graphitization. The CVD reaction took place in a 2.54 cm quartz tube with the pure silicon material held in an alumina boat placed in the center of the tube furnace's heating region.

For anode production, the CVD processed materials are mixed in deionized water with carboxymethyl-cellulose (CMC, Sigma Aldrich), which acts as a binder, and spread across 90 mm by 30 mm copper foil with a doctor blade coater. The anode is then vacuum dried at 90 °C for 12 h. Circular anodes 12.5 mm in diameter are then punched out of the foil and measured to learn the precise anode weight loading per coin-cell. Coin-cell assembly takes place within an argon filled glovebox, using 2032 stainless steel coin-cell components from MTI. The acting cathode is a 1 mm thick 12.4 mm diameter disk of metallic lithium from Alpha Aesar, with a 25 μm trilayer polypropylene-polyethylene-polypropylene membrane separator, and a 9:1 volume composition of lithium hexafluorophosphate ($LiPF_6$):fluoroethylene carbonate (FEC) as the acting electrolyte.

Chemical analysis is performed on the active anode materials through an FEI NNS450 scanning electron microscope (SEM) and energy dispersive x-ray spectrometer (EDS). The elemental analysis provided by the EDS measurements and the measured coin-cell weight loading is then used to calculate the theoretical capacity of these batteries and their respective 'C rate', i.e. the current required to fully charge or discharge the anode within an hour. The coin-cells are tested on a Neware BTS 4000, set to perform five cycles at 0.1 C from 1.5 V to 0.05 V for anode 'formation', a standard industry process allowing for slow development of a SEI that will permit cycling stability. Upon completing the formation cycles the battery testing system then cycles the half-cells at 0.5 C until adequate data is collected.

Four silicon synthesis conditions are chosen for a direct comparison of their electrochemical performance. The tested samples were all prepared at a pressure of 526 Pa (4 Torr), 100 sccm of precursor mixture, and a 50% pulsing duty cycle. One of the samples is produced under continuous conditions, while the others are produced with 3, 12.5 and 25 pulses per residence time (corresponding to 30, 125 and 250 Hz pulsing frequency). All the samples undergo the same CVD coating, anode production, battery assembly, and half-cell testing processes described above. The anode weight loading is consistently between 1.0 and 1.21 mg cm^{-2} for all the tested samples.

3. Computational details

The coagulation of nanoparticles in both the plasma and its afterglow is modeled using the governing equation from [19]:

$$\frac{\mathrm{d}N_i^p}{\mathrm{d}t} = \frac{1}{2}\sum_{q=-\infty}^{\infty}\sum_{j=1}^{i-1}\beta_{i-j,j}^{p-q,q}N_{i-j}^{p-q}N_j^q - \sum_{(q=-\infty)}^{\infty}\sum_{(j=1)}^{(i-1)}\beta_{i,j}^{p,q}N_i^pN_j^q \tag{1}$$

where $N_i{}^p$ is the number density of particles with volume v_i and charge p. The indexes i and j refer to the particle volume, which is assumed to be an integer multiple of the primary particle volume. For the results discussed here, the primary volume is the one corresponding to a particle with a diameter of 8 nm. This choice is motivated by experimental measurements, which suggest that the particle average diameter is 8 nm with a narrow size distribution for a continuous plasma operating at a pressure of 526 Pa (4 Torr). The indexes p and q refer to the number of elementary charges on each particle. The coefficient β accounts for the rate of coagulation as a function of both size and charge of the collision partners. It can be written as:

$$\beta_{i,j}^{p,q} = Q_{i,j}^{p,q}\beta'_{i,j} \tag{2}$$

where $\beta'_{i,j}$ is the coagulation coefficient for neutral particles of volumes v_i and v_j, in the free molecular regime [20]:

$$\beta'_{i,j} = \left(\frac{3}{4\pi}\right)^{\frac{1}{6}}\left(\frac{6k_\mathrm{B}T_\mathrm{gas}}{\rho}\right)^{\frac{1}{2}}\left(\frac{1}{v_i}+\frac{1}{v_j}\right)^{\frac{1}{2}}\left(v_i^{1/3}+v_j^{1/3}\right)^2. \tag{3}$$

Here ρ is the particle material density (2330 kg m^{-3} for silicon), k_B is the Boltzmann constant and T_gas is the gas temperature. The term $Q_{i,j}{}^{p,q}$ accounts for the electrostatic interaction between colliding nanoparticles and it is written as [20]:

$$Q_{i,j}^{p,q} = \begin{cases} \exp\left(-\dfrac{pqe^2}{4\pi\epsilon_0 R_{s,ij}k_\mathrm{B}T_\mathrm{gas}}\right) \text{if } p\cdot q > 0 \\ -\dfrac{pqe^2}{4\pi\epsilon_0 R_{s,ij}k_\mathrm{B}T_\mathrm{gas}} \quad \text{if } p\cdot q \leqslant 0 \end{cases} \tag{4}$$

where e is the elementary charge and ε_0 is vacuum permittivity. This term induces an increase in the agglomeration rate for particles of opposite charge, and a reduction in agglomeration rate for particles of the same charge. $R_{s,ij}$ has the following expression:

$$R_{S,ij} = \left(\frac{3}{4\pi}\right)^{1/3} \left(v_i^{1/3} + v_j^{1/3}\right). \tag{5}$$

Equation (1) is coupled to the following equation that accounts for the charging of nanoparticles, both in the plasma and in the afterglow, because of collision with electrons, ions and metastables:

$$\frac{\mathrm{d}N_i^p}{\mathrm{d}t} = -\left(\nu_e^{i,p} + \nu_i^{i,p} + \nu_M^i\right) N_i^p + \nu_e^{i,p+1} N_i^{p+1} + \left(\nu_i^{i,p-1} + \nu_M^i\right) N_i^{p-1} \tag{6}$$

where $\nu_i^{i,p}$ is the collision frequency between electrons and a particle with volume v_i and charge p, $\nu_i{}^{i,p}$ is the collision frequency between ions and a particle with volume v_i and charge p, and ν_M^i is the collision frequency between argon metastables and a particle with volume v_i. For electrons, the rate of nanoparticle charging is determined using the orbital motion limited (OML) theory [21–23]:

$$\nu_\mathrm{e}^\mathrm{i,p} = \begin{cases} n_\mathrm{e}\pi R_\mathrm{p,i}^2 \upsilon_\mathrm{e,\,th} \exp\left(\frac{eV_\mathrm{p,i}}{k_\mathrm{B}T_\mathrm{e}}\right) & \text{if } V_\mathrm{p} < 0 \\ n_\mathrm{e}\pi R_\mathrm{p,i}^2 \upsilon_\mathrm{e,\,th} \left(1 + \frac{eV_\mathrm{p,i}}{k_\mathrm{B}T_\mathrm{e}}\right) & \text{if } V_\mathrm{p} \geqslant 0 \end{cases} \tag{7}$$

where n_e is the electron density, $R_\mathrm{p,i}$ is the radius of a particle with volume v_i, $\upsilon_\mathrm{e,th}$ is the electron thermal velocity, T_e is the electron temperature and $V_\mathrm{p,i}$ is the particle floating potential, equal to ${}^{ke}/_{4\pi\epsilon_0 R_{p,i}}$ with k being the number of elementary charges carried by the particle. For ions, we use the expression from Gatti and Kortshagen to account from deviations from the OML theory due to ion collisions with the backgroun gas [24]:

$$\nu_\mathrm{i}^\mathrm{p} = \begin{cases} n_\mathrm{i}\pi R_\mathrm{p}^2 \upsilon_\mathrm{i,\,th} \exp\left(-\frac{eV_\mathrm{p}}{k_\mathrm{B}T_\mathrm{i}}\right) & \text{if } V_\mathrm{p} \geqslant 0 \\ P_0\nu^\mathrm{OML} + P_1\nu^\mathrm{CE} + P_2\nu^\mathrm{HY} & \text{if } V_\mathrm{p} < 0 \end{cases} \tag{8}$$

where n_i is the ion density, $\upsilon_\mathrm{i,th}$ is the ion thermal velocity, and T_i is the ion temperature. ν^OML, ν^CE, ν^HY are the ion-nanoparticle collision frequency in the OML (collisionless) limit, for the collision-enhanced regime, and for the hydrodynamic limit, respectively. P_0, P_1 and P_2 are weights that depend on the particle Knudsen number. For the exact expression of these terms, we refer the reader to [24]. We have found that utilizing this expression for the ion collection frequency makes a significant difference in the average particle charge for a given plasma condition, reducing by roughly 50%. This is to be expected, given the relatively high pressure at which the experiments are performed and the calculations are run (526 Pa). We calculate the Knudsen number $\lambda_\mathrm{i}/R_\mathrm{p}$ (with λ_i being the ion mean free path) to be $\sim$1000 for a 8 nm particle, sufficiently small to lead to a deviation from OML theory. The ion mean free path is estimated to be 4.7 μm at 526 Pa (4 Torr), based on the ion mobility data from [25]. We assume the dominant ion to be H_3^+ [26, 27]. At 526 Pa, the ion mobility is 1038.8 cm^2 (V s^{-1}) and the ion diffusion coefficient is 26.84 cm^2 s^{-1}.

The charging frequency due to collisions between a particle with volume v_i and metastable argon atoms is equal to:

$$\nu_\mathrm{M}^i = n_\mathrm{M}\pi R_{p,i}^2 \upsilon_\mathrm{M,\,th}. \tag{9}$$

With n_M equal to the argon metastable density and $\upsilon_\mathrm{M,th}$ being the metastable thermal velocity. n_M is the sum density of the $1\mathrm{s}_5$ and $1\mathrm{s}_3$ metastable states (in Paschen notation) at energies of 11.548 eV and 11.723 eV, respectively. The metastable translational temperature is assumed to be equal to the gas temperature.

This basic set of equations is solved in two different ways depending on whether the 'plasma on' or the 'afterglow' phase is modeled. For the 'plasma on' phase, the ion density, metastable density and electron temperature are kept constant and equal to values obtained from the literature. The ion density is $n_\mathrm{i} = 10^{11}$ cm^{-3} and the electron temperature T_e is equal to 4 eV [28]. The metastable density is has been reported to be as high as 2×10^{11} cm^{-3} for the case of a low-temperature dusty plasma with carbon particles dispersed within it [16]. Interestingly, the metastable density has not been measured for the case of a flow-through, silicon nanoparticle-producing plasma such as the one used here. In the model, we have varied the metastable density between 10^8 cm^{-3} and 10^{13} cm^{-3} to investigate its role on the charging dynamics. The electron density is calculated by assuming quasineutrality, i.e. $n_\mathrm{i} = n_\mathrm{e} + kn_\mathrm{p}$ with n_p being the total nanoparticle density equal to $\sum_{p=-\infty}^{\infty}\sum_{i=0}^{\infty} N_i^p$.

In the 'afterglow' phase, the electron, ion and metastable densities decay in time with a rate calculated using the collection frequencies in equations (7)–(9). Quasineutrality is not strictly applied in the afterglow. In addition, diffusional losses of charge carriers to the reactor walls are accounted for by using effective electron and ion diffusion coefficients. These are calculated using the approach outlined in [12, 29]. In short, the electron and ion diffusion coefficients are equal to the ambipolar diffusion coefficient, $D_\mathrm{i}(1 + T_\mathrm{e}/T_\mathrm{i})$ with D_i being the ion diffusion coefficient, in the early phase of the afterglow. Later in the afterglow, the electron and ion diffusion coefficients diverge following the trend shown in figure 1 of [12]. The critical parameter that controls the transition is the ratio between the electron debye length and the system characteristic diffusion length, equal to $R/2.404$ for a cylindrical system, with R being the inner reactor radius (10 mm in our case). This approach allows to transition smoothly from an ambipolar diffusion regime early in the afterglow, to a free diffusion regime late in the afterglow when electrons cool and the debye length increases.

We make the reasonable assumption that ion and metastable temperature are in equilibrium with the gas temperature. The electron temperature is calculated by assuming that each electron lost to either the reactor wall or to the nanoparticles carries with it an average energy of $2k_\mathrm{B}T_\mathrm{e}$ [30]. We assume that the electron temperature cannot decay below the gas temperature in the afterglow, i.e. T_e has a floor value equal to T_gas.

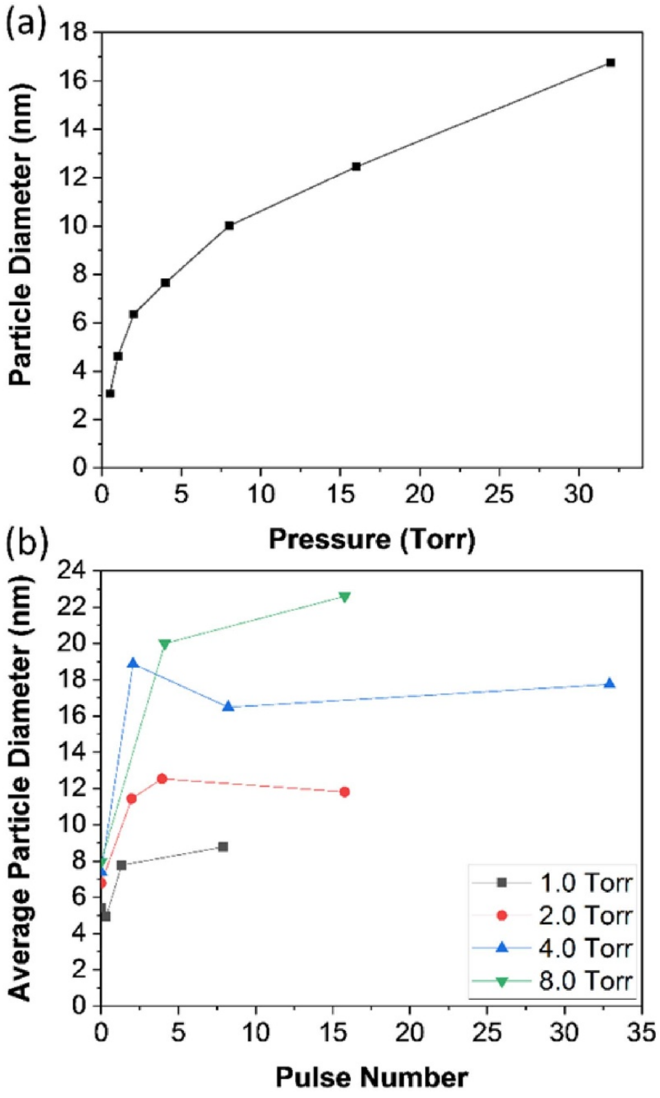

Figure 1. (a) Average particle diameter as a function of reactor pressure for a continuous plasma. (b) Average particle diameter at various pressure, as a function of number of plasma pulses per residence time. The duty cycle is 50% for all these measurements. The diameters reported in this figure are based on XRD measurements and Scherrer's analysis.

This set of equations is discretized and integrated in time using an explicit scheme with an adaptive time step. The initial time step is set to 10 ns, and its value can increase by up to a factor of 5 depending on the rate of change in the electron density value. This captures the need for a shorter computational time step earlier in the 'plasma on' phase when particles are charging and the electron density is decaying, as well as earlier in the 'afterglow' phase when the particle charge is neutralizing and the plasma density is decaying.

As initial conditions, we use monodispersed particles with a diameter of 8 nm and without charge. First, the 'plasma on' phase is calculated until a steady state in average particle charge and in electron density is reached. This occurs within 10 μs. The plasma is then turned off and the model switches to the 'afterglow' case.

For the results discussed in this manuscript, we used a total of 14 charge bins (from -8 to $+5$ charges per particle) and 12 volume bins (from a 8 nm particle to a 18.315 nm particle).

4. Results and discussion

Figure 1(a) summarizes the dependence of the average particle diameter on the reactor pressure, for the case of a continuous plasma. The total flow rate is constant and equal to 100 sccm (1.37% silane in argon). An increase in reactor pressure induces an increase in particle size, going from <5 nm at 131.5 Pa (1 Torr) to 16 nm at 4210 Pa (32 Torr). Unfortunately, we have also reproducibly observed a significant drop in particle yield at higher operating pressures, going from $\sim$50 mg h at 526 Pa (4 Torr), corresponding to a 50% silane-to-particle conversion rate, to $\sim$5 mg h at 4210 Pa (32 Torr), making this approach challenging for applications requiring large yields. In figure 1(b), we show the variation in particle diameter at different reactor pressures, but comparing the continuous mode (zero pulse) to pulsed mode with varying number of pulses per residence time. The duty cycle was 50% for all of these samples. Given the residence time of 100 ms, based on flow velocity, the 3, 12.5 and 25 pulses per residence time correspond to pulsing frequencies of 30 Hz, 125 Hz and 250 Hz, respectively. We should point out that we have also observed a decrease in mass yield for the pulsed case compared to the continuous case, although that drop is less severe (from $\sim$50 mg h to $\sim$30 mg h). The average particle diameters for figure 1 have been obtained by XRD measurements, using Scherrer analysis to estimate the crystal size. From figure 1(b), it is clear that operating the plasma in pulsing mode has important consequences on the particle size, with even three pulses inducing a significant increase in diameter. Figure 2(a) shows the particle size distribution for the continuous and for the pulsed cases, with figures 2(b)–(e) showing some representative TEM micrographs. The TEM analysis is in good agreement with the average particle diameters obtained by XRD and shown in figure 1. For the continuous case, the average particle diameter is 8 nm and the size distribution is narrow, in agreement with previous reports suggesting that electrostatic stabilization while in the plasma prevents particle agglomeration [17]. Even with three pulses per residence time, the average particle size increases significantly to almost 20 nm. The size distributions for the pulsed cases is still relatively narrow, with very few particles in the 50–100 nm range and no particles above 100 nm in size.

After silicon production we have proceeded to investigate the effect of pulsing on the electrochemical performance of the materials when used as anodes for lithium-ion batteries. The samples shown in figure 2 were processed according to the procedure outline in the experimental details section of this manuscript. In short, it is important to coat the silicon with a carbon protective layer to enhance their electrochemical performance. Moreover, it is preferable to achieve a high degree of graphitization of the carbon shell to improve the electrical transport properties of the anode [6]. This can be achieved by the two-steps CVD and graphitization process that our group

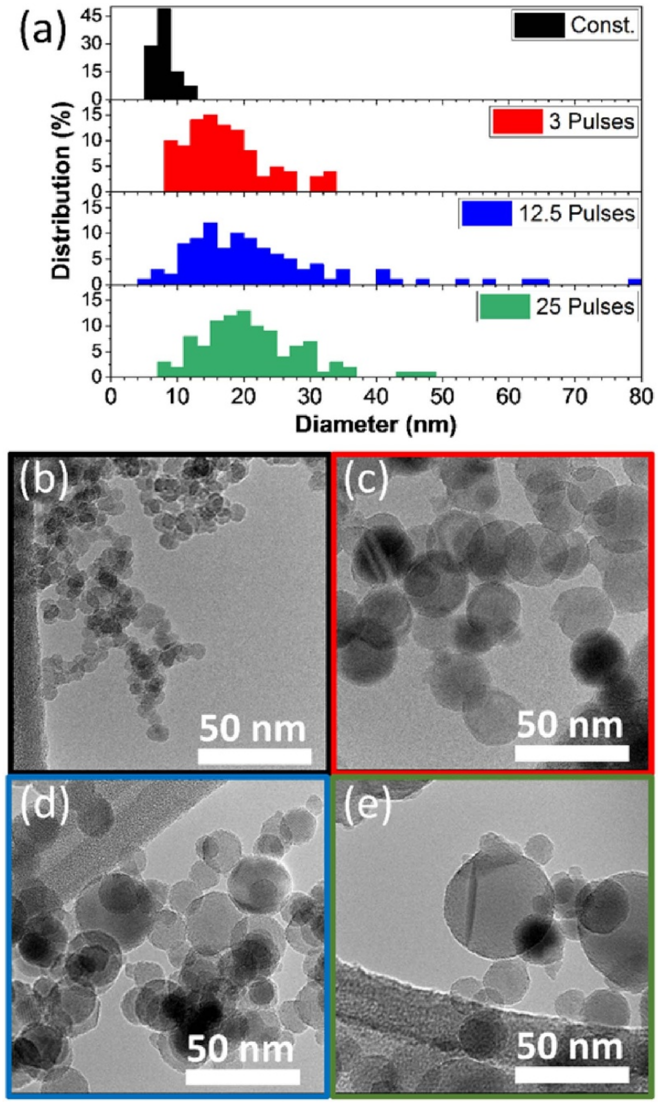

Figure 2. (a) Particle size distributions for the continuous and pulsed cases, as obtained by analyzing several TEM micrographs. (b)–(e) Representative TEM micrographs for particles produced with a continuous plasma, or with 3, 12.5 and 25 pulses per residence time, respectively.

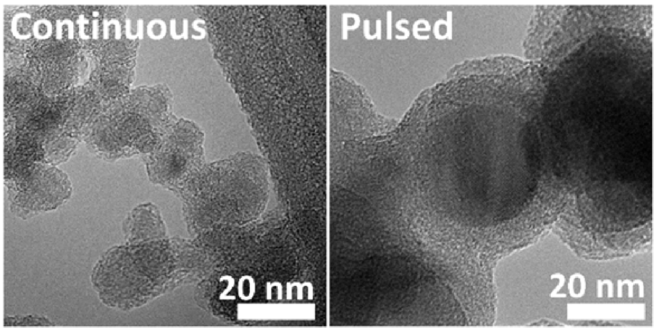

Figure 3. TEM micrographs of silicon particles produced using a continuous (left) or pulsed (right) mode, after coating with a graphitized carbon shell.

has previously described in details [6]. The same technique is used to process the silicon particles discussed here. TEM micrographs for particles produced in continuous and pulsed modes, after carbon coating, are shown in figure 3. The silicon cores appear enclosed in a conformal carbon layer. Elemental analysis perform via SEM suggest that the silicon-to-carbon ratio is between 0.6 and 0.7 for the pulsed samples, by weight. The ratio is significantly smaller (0.24) for the particles produced with a continuous plasma. All the samples are processed using identical CVD parameters in terms of process time, temperature and pressure. The fact that a comparatively thicker carbon layer is grown on the smallest particles, with the same processing condition, hints at a curvature dependence on the carbon growth kinetics.

The sample electrochemical characterization is summarized in figure 4. Figure 4(a) shows the cycling data for the four samples shown in figure 2. The sample produced with a pulsing plasma have a gravimetric capacity of between 1000 and 1400 mAh g^{-1}. They show reasonable stability, with <10% capacity loss over the 1st 60 charge–discharge cycles. The sample produced with a continuous plasma has significantly lower capacity, around 400 mAh g^{-1}. This is expected given the significantly lower content of silicon in the sample. The cycling stability for this sample is very good. Figure 4(b) shows the variation in Coulombic efficiency over number of cycles for the four samples. The samples produced with a pulsing plasma have a 1st cycle efficiency of $\sim$74%, while the sample produced with a continuous plasma has a significantly lower 1st cycle efficiency (<50%). This confirms that even a relatively small change in particle size (from 8 nm to 20 nm) has profound effects on the anode performance, and that this application is particularly sensitive to particle size. All samples show good stability, likely because there are no large particles (close to 150 nm or above) in these samples.

Overall, these data confirm that it is desirable to achieve a precise control on the size distribution of silicon particles, as their performance as anode material in lithium-ion batteries is strongly affected by it. A simple approach such as pulsing of the RF power has important consequences on the particle size, even at seemingly low pulse rates.

To better understand how pulsing affects the kinetics of coagulation in this system, we have performed a series of computational experiments using the modeling approach outlined earlier in the computational details section. Figure 5 shows the modeled variation in critical parameters during the ‘plasma on’ and ‘afterglow’ phases of the process. During the ‘plasma on’ phase (figure 5(a)), the initially neutral aerosol is charged and acquires an average negative charge of ~ -1.45. The ion density is kept constant during this phase. The electron density rapidly decays as more negative charge is carried by the particles. The nanoparticle density remains stable and close to its initial value. This value is calculated using the experimentally measured mass production rate ($\sim$50 mg h) for the case of 8 nm particles produced in the continuous plasma. The system reaches steady state rapidly, well within 10 μs. After steady state is reached, the model switches to the ‘afterglow’ phase, with results summarized in figures 5(b) and (c). For this plot, a single afterglow with a total duration of 20 ms is considered.

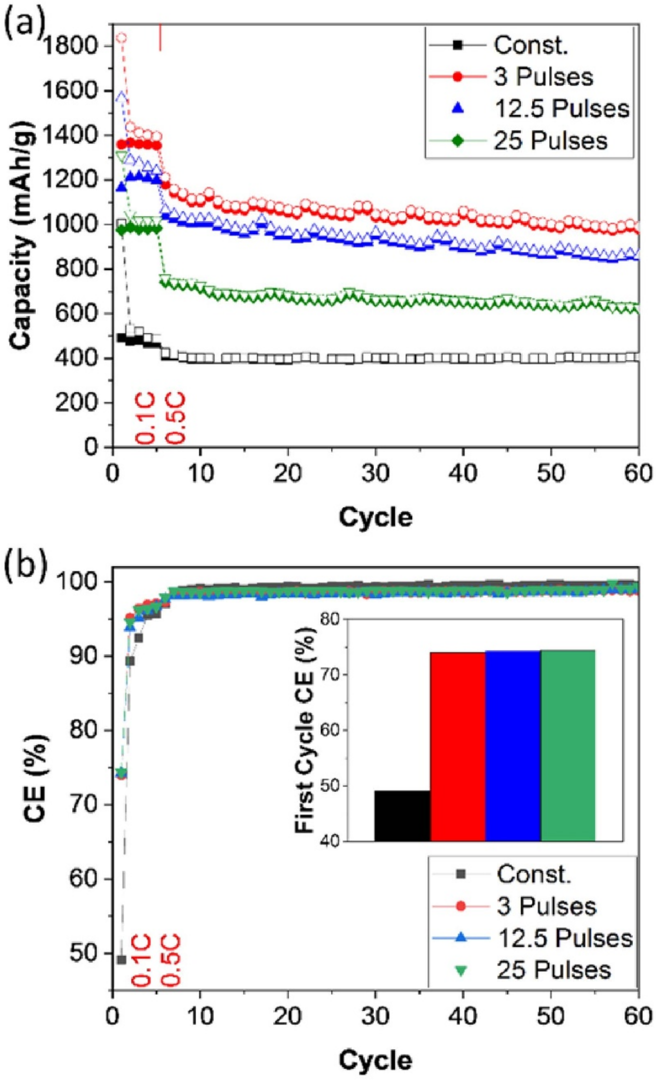

Figure 4. (a) Gravimetric capacity vs cycle number for the samples produced with a continuous plasma and at varying pulsing frequencies. The charging rate is kept at 0.1 C for the 1st five formation cycles, then increased to 0.5 C. (b) Same as (a) but showing the Coulombic efficiency vs. cycle number. In the inset we summarize the first cycle efficiency for the samples.

The metastable density is assumed to be 10^{12} cm^{-3} for these plots. Figure 5(b) shows the decay of charge carriers and argon metastables as a function of time. It should be noted that the electron and ion densities are plotted on two different y-axes, for clarity. The ion density drop considerably with 100 μs. The electron density has a more complex time dependance. This is due to the presence of long-lived argon metastables, which continuously supply electrons to the reaction volume by ionizing collisions with the nanoparticles. These trends are in good agreement with previous modeling results and measurements of metastable lifetime in afterglows, which are well know to be several microseconds [10, 15, 16]. Measurement of the electron density decays in dusty plasma afterglows are also consistent with these computational result [31]. The electron temperature decays from its initial value of 4 eV to its floor value, equal to the gas temperature, within 50 μs. It should be mentioned that we assume that the electrons supplied late in the afterglow because of nanoparticle-metastable collisions are assumed to be 'cold', meaning at a temperature equal to the gas temperature. We also neglect metastable pooling effects, which could both induce a more rapid decay in the metastable density but also result in electron heating due to the formation of energetic electrons after metastable–metastable collisions. This assumption is justified by the relatively slow kinetic of the metastable pooling reaction compared to quenching at the nanoparticle surfaces, which we estimate to be the dominant quenching mechanism even for metastable densities as high as 10^{12} cm^{-3} when using the pooling reaction rate from [15] (6.2×10^{-10} cm^3 s^{-1}). Also shown in figure 5(c) are the nanoparticle density and average nanoparticle charge. The density drops by roughly a factor of 2 within 20 ms, while the average charge relaxes from the negative value acquired in the plasma to zero in less than a millisecond. After this relaxation phase, the charge becomes quasi-steady-state, with a visible increase to a small positive value around 10 ms of afterglow time. This is likely due to the transition from ambipolar to free diffusion regime, which induces a loss of electrons at the reactor walls.

We have found that electrostatic effects enhance the agglomeration of particles in the afterglow. These effects are dependent on the shape of the charge distribution in the quasi-steady-state phase of the afterglow (after ∼1 ms), which in turn is dependent on various process parameters. Here in particular we discuss the importance of metastable density and gas temperature on the coagulation dynamics in the afterglow. The dependece on the metastable density is summarized first in figures 6(a) through (d). For these computation experiments, the gas temperature is kept at 300 K, and the ion density and electron temperature are kept at the same values specified before (10^{11} cm^{-3} and 4 eV, respectively). The metastable density is varied between 10^8 cm^{-3} and 10^{13} cm^{-3}. Admittedly, the 10^{13} cm^{-3} value is probably unrealistic, although values exceeding 10^{11} cm^{-3} have been reported for the case of an argon plasma with carbon nanodust dispersed within it [16]. Figure 6(a) shows the variation in nanoparticle density in the afterglow for the two limiting values of metastable density. The higher metastable density leads to a faster decrease in nanoparticle density. The charge distributions after 2 ms in the afterglow are shown in figure 6(b). The higher metastable density leads to a broader charge distribution, in particular with a higher fraction of positive particles. We choose to use two quantities to describe the shape of the particle charge distribution: the ratio between the densities of particles with charge +1 and charge −1 (Q_{+1}/Q_{-1}) and the ratio between the particles with charge +1 and the non-charged particles (Q_{+1}/Q_0). The 1st parameter describes how symmetric is the distribution, and the 2nd provides information on its width. As shown in figure 6(c), Q_{+1}/Q_{-1} remains close to 1 over the range of considered metastable densities, although it increases to 2.5 for the maximum density value. Q_{+1}/Q_0 progressively increases as the metastable density increases. These two descriptors correlate well with the dependance of nanoparticle density and size with the metastable density, as shown in figure 6(d). This is reasonable, as a broader charge distribution is expected to lead to a more significant electrostatic

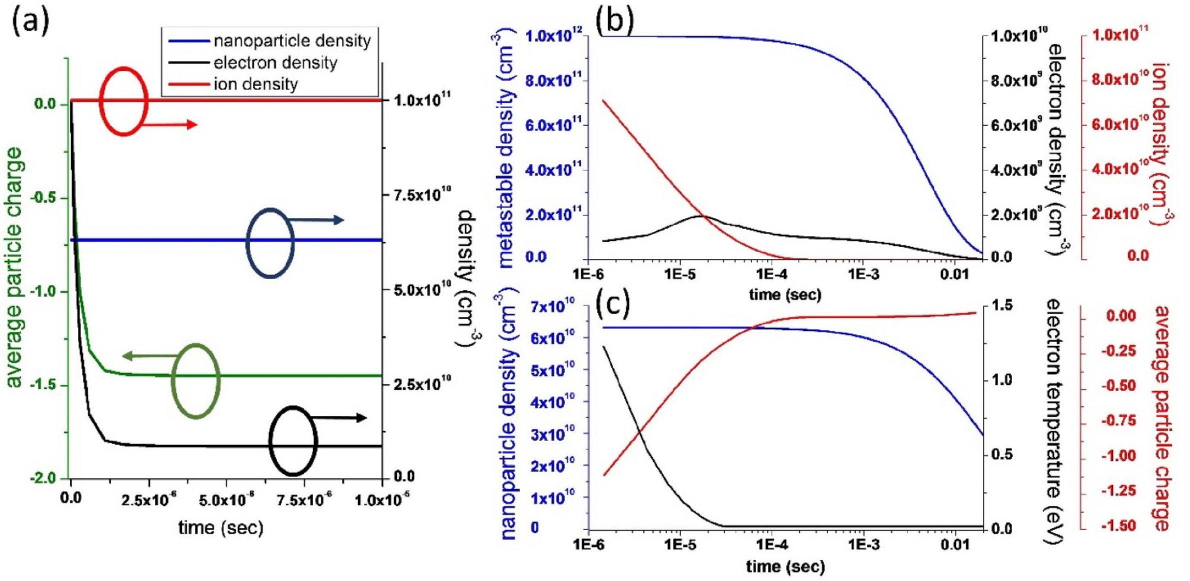

Figure 5. (a) Time variation of ion, electron and nanoparticle densities, together with the average particle charge, during the 'plasma on' phase. (b) Time variation of ion, electron and metastable densities in the plasma afterglow. (c) Same as (b), but showing the nanoparticle density, the electron temperature and the average particle charge. Please note that the *x*-axis is on a logarithmic scale for plots (b) and (c).

enhancement of the coagulation rate in the afterglow. Interestingly, the gas temperature also has an effect the charge distribution in the afterglow, as summarized in figures 6(e)–(h). Increasing the gas temperature from 300 K to 1000 K leads to an increase in the agglomeration rate and a faster drop in nanoparticle density (see figure 6(e)). The charge distribution at 1000 K appears to be wider than at 300 K, as shown in figure 6(f) and as confirmed by the variation of the Q_{+1}/Q_{-1} and Q_{+1}/Q_0 parameters (figure 6(g)). Figure 6(h) indeed shows how the increase in temperate progressively increases the particle size and decreases the particle density after 20 ms in the afterglow.

This dependence can be theoretically predicted by writing an expression for the fraction of particles with zero charge, F_0:

$$\frac{\mathrm{d}F_0}{\mathrm{d}t} = -\left(\nu_\mathrm{M} + \nu_\mathrm{e}^0\right) F_0 + \nu_\mathrm{M} F_{-1} + \nu_\mathrm{e}^{+1} F_{+1} \tag{10}$$

where ν_M is the charging frequency due to metastable collisions, ν_e^0 and ν_e^{+1} are the electron collection frequencies for a neutral and a positive particle respectively, and F_{-1} and F_{+1} are the fraction of particles with charges -1 and $+1$, respectively. Here we neglect the role of positive ions, since we are considering the later stage of the afterglow after the ion density has decayed. Since the charge distribution is near steady state after the initial transient, and approximating its shape to be symmetric (meaning $F_{+1} \approx F_{-1}$), we then find:

$$\frac{F_{+1}}{F_0} = \frac{\nu_\mathrm{M} + \nu_\mathrm{e}^0}{\nu_\mathrm{M} + \nu_\mathrm{e}^{+1}}. \tag{11}$$

This relation explains why an increase in the metastable density leads to a broadening of the particle charge distribution in the afterglow, since this leads to an increase in ν_M. In addition, and increase in temperature also leads to a broadening of the charge distribution because the charging frequencies ν_e^0 and ν_e^{+1} are related by the following, according to OML theory:

$$\nu_\mathrm{e}^{+1} = \nu_\mathrm{e}^0 \left(1 + \frac{eV_\mathrm{p}}{k_\mathrm{B} T_\mathrm{e}}\right). \tag{12}$$

This implies that an increase in electron temperature in the afterglow brings their ratio closer to one, widening the particle charge distribution and enhancing the particle coagulation rate. We remind the reader that for simplicity we assume that the electron temperature has a floor value equal to the gas temperature. Therefore, varying the gas temperature also affect the electron temperature late in the afterglow. We assume that electrons emitted from particles after collision with a metastable are 'cold' (i.e. 300 K). A more precise description of the electron temperature and of the degree of non-thermal equilibrium in the late afterglow is needed to model the coagulation dynamics with greater precision. Indeed more refined simulations have shown that the electron temperature can exceed the gas temperature by more than one order of magnitude even after 1 ms in the afterglow, because of long-lived metastables [11, 13]. With respect of gas (neutral) temperature, a value of 1000 K is probably excessively high for this system, although it is also well-known that the assumption that the gas temperature stays at 300 K is simplistic [14]. There is a need of more precise experimental measurements of both the metastable density and the gas temperature in this system, as they affect the particle agglomeration dynamics.

Finally, in figure 7 we show the result of a computational experiment in which the system is pulsed ten times. While in the experiment we use a 50% duty cycle (meaning the plasma on time is equal to the afterglow time), for the sake of reducing computational time the plasma is kept on only for 10 μs

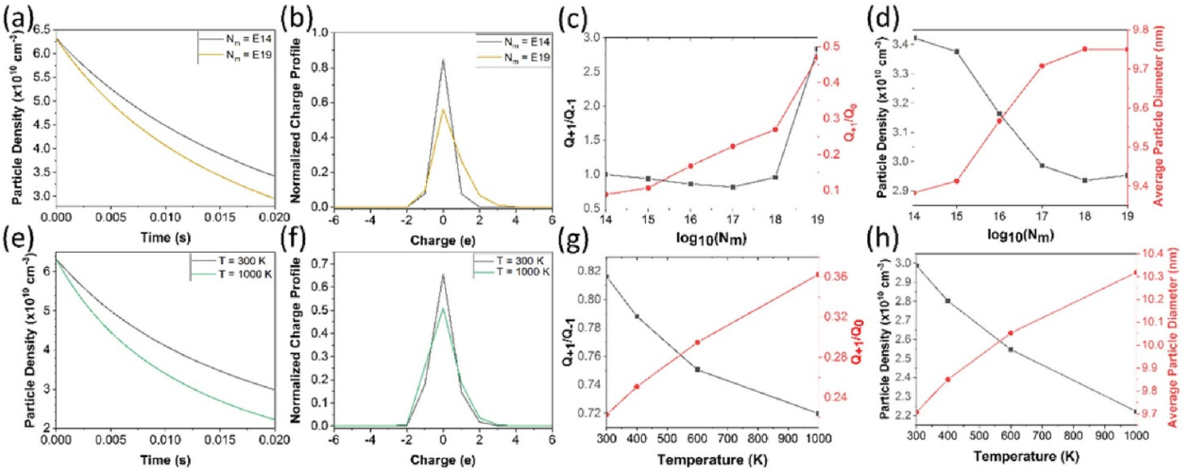

Figure 6. (a) Evolution of total particle densities in the afterglow for initial metastable densities of 10^8 cm^{-3} and 10^{13} cm^{-3}. (b) Corresponding particle charge distributions in the afterglow, after the initial charge relaxation transient. (c) Dependence of the Q_{+1}/Q_{-1} and Q_{+1}/Q_0 parameters on the initial metastable density. (d) Dependence of particle size and density on the initial metastable density. (e) Evolution of total particle density in the afterglow for gas temperature of 300 K and 1000 K. (f) Corresponding particle charge distributions in the afterglow, after the initial charge relaxation transient. (g) Dependence of the Q_{+1}/Q_{-1} and Q_{+1}/Q_0 parameters on the gas temperature. (h) Dependence of particle size and density on the gas temperature.

per pulse, as this is more than sufficient for the system to reach steady state. Figure 7(a) shows the evolution of particle density over the sum of ten afterglows, each with a 2 ms duration. The result is compared to the case in which the plasma is kept on for 20 ms (continuous case) and for the case of a neutral aerosol with same initial average size and density as for the plasma cases. Pulsing of the plasma leads to a clear decrease in nanoparticle density compared to the continuous plasma case, consistent with the experimental result. Moreover, pulsing leads to an enhanced particle agglomeration compared to the neutral case in which any electrostatic enhancement of the agglomeration rate is absent. Figure 7(b) and (c) show a 2D plot of the particle density as a function of size (*x*-axis) and charge (*y*-axis) after the last plasma on phase and after the last afterglow, confirming that the charge relaxes to zero in the afterglow and the density at large particle sizes increases.

While the data discussed so far suggests that the bipolar charge distribution in the afterglow enhances the agglomeration kinetics compared to the neutral case, our modeling results are still only in qualitative agreement with the experimental data. Given a 100 ms residence time in the experiment, the 25 pulses case at 50% duty cycle corresponds to a duration of 2 ms for the plasma on and afterglow phases. In the total afterglow time (50 ms) the size grows from 8 nm to 20 nm, leading to a drop in nanoparticle density by a factor of more than 15. Various reasons may contribute to the quantitative disagreement between our model results and the experimental data. As recently shown by Chen and Hogan [10], the thermal desorption of negative charges from the particles may have an important effect on both the average particle charge in the plasma and on the charge distribution in the afterglow. Indeed, recent measurements from our group have shown that electron emission from nanoparticles may affect the overall charge balance in the discharge [32], although that is measured at considerably lower pressures than the ones used here. The reduced heat loss to the background gas at lower pressure leads to an increase in particle temperature, making electron desorption more likely. There is also significant uncertainty on the value of energy barrier that should be used to estimate the emission current. In our previous work, the emission current was estimated via the Richardson Dushman equation using the material work function in the exponential term, reduced by the Coulombic potential of the charges present on the particle [33]. This value is typically a few eVs. Chen and Hogan use significantly lower energy barriers [10], with values of either 0.6 eV as derived in [34], or 1 eV based on the measurements reported in [35]. In addition, there is also uncertainty in the temperature that nanoparticles attain in these systems, while in the plasma. Theoretical predictions suggest that the particle temperature can be few hundreds of degrees higher than the gas temperature while in the plasma [28, 36], although these models have not been applied to the afterglow case and do not include any heating from interaction with argon metastables. Finally, plasma-induced heating effects and cooling to the background gas both scale like the particle surface area, making the steady-state temperature size-independent. On the other hand, under unsteady conditions the particle cooling rate is proportional to the particle surface-to-volume ratio, i.e. they scale like $1/R_p$. This indicates that particles of different sizes will cool and desorb negative charges at different rates in the plasma afterglow, leading to a potential coupling between particle charge and size distributions. A more in depth investigation of these aspects is left for a future study.

We should also point out that we have only observed spherical, single-crystal nanoparticles in our TEM analysis of the samples produced via plasma pulsing. This suggests that the particles agglomerates, formed during the afterglow, most likely experience rapid sintering in the subsequent ‘plasma

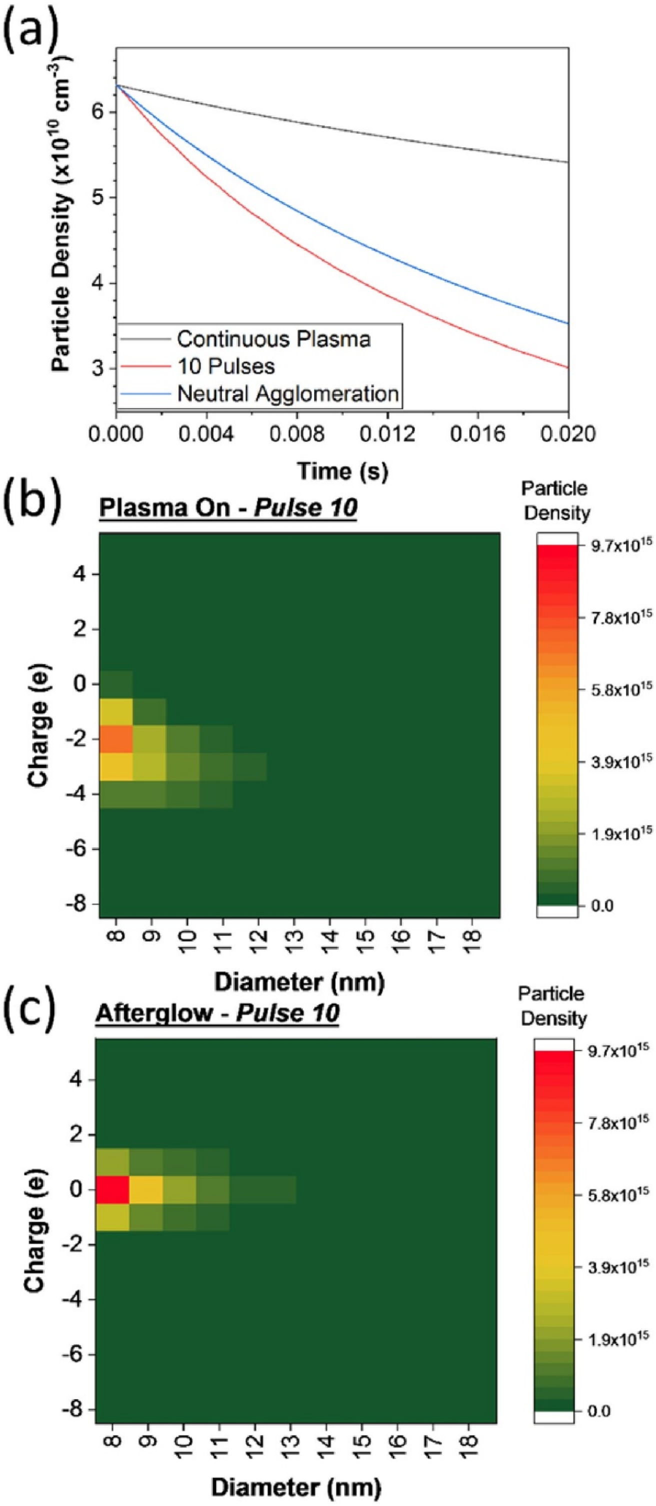

Figure 7. (a) Calculated cumulative effect of ten plasma pulses on the total particle density, compared to the case of a continuous plasma and the case of free-molecular agglomeration, without any electrostatic effects. (b), (c) Two dimensional plots of particle densities as a function of size and charge after the last 'plasma on' pulse and after the last afterglow, based on the computational approached described in this manuscript.

on' phase. An estimate of the temperature needed to achieve complete sintering within the duration of the plasma pulse can be obtained using the following formula [37–39]:

$$\tau_{\text{sinter}} = \frac{3k_{\text{B}}T_{\text{P}}N}{64\pi D\left(T_{\text{P}}\right)\sigma} \tag{13}$$

where τ_{sinter} is the sintering time, T_{P} is the particle temperature, N is the number of atoms in the particle, $D(T_{\text{P}})$ is the self-diffusion coefficient and σ is the surface tension. Using a surface tension value of 0.826 J m^{-2} [37] and a self-diffusion coefficient of $4.69 \times 10^{-7}\exp(-7562/T)$ m^2 s^{-1} [38], we find that two ~16 nm particles can sinter into a ~20 nm particle within 2 ms at a temperature τ_{sinter} of 470 K. This temperature increase to 575 K for two ~40 nm particles to give a ~50 nm particle. These temperature values are reasonable given the theoretical estimates of particle temperatures in plasmas that can be found in the literature [28, 36], and in agreement with our observation of single-crystal spherical particles.

5. Conclusions

While low-temperature plasmas are capable of producing ultra-fine particles with excellent precursor utilization, excessively small nanoparticles are actually detrimental for applications such as for lithium-ion battery materials. For the case of silicon, very small particles have too large of a surface area, reducing the 1st cycle Coulombic efficiency upon lithiation. This manuscript demonstrates that operation in a pulsed mode is a simple approach to significantly increase the average particle size (from ~8 to ~20 nm) and improve the electrochemical performance in anodes for lithium-ion batteries. The zero-dimensional model described here predicts that electrostatic effects enhance the particle coagulation rate in the afterglow due to the transition from a dominantly negative to a bipolar nanoparticle charge distribution. The width of the charge distribution, and in turn the coagulation rate in the afterglow, depends on parameters such as metastable density in the plasma, gas temperature, and electron temperature in the afterglow. All of these parameters are still poorly characterized for the case of flow-through reactor, in argon–silane mixtures. Advances in both the experimental characterization of these systems and in their modeling is needed to achieve a better agreement between plasma aerosol models and the measured increase in particle size during pulsed operation.

Data availability statement

The data generated and/or analyzed during the current study are not publicly available for legal/ethical reasons but are available from the corresponding author on reasonable request.

Acknowledgment

This work has been supported by the US National Science Foundation under Award Number 1940952.

ORCID iD

Lorenzo Mangolini https://orcid.org/0000-0002-0057-2450

References

[1] Kortshagen U R, Sankaran R M, Pereira R N, Girshick S L, Wu J J and Aydil E S 2016 Nonthermal plasma synthesis of nanocrystals: fundamental principles, materials, and applications *Chem. Rev.* **116** 11061–127

[2] Mariotti D and Sankaran R M 2010 Microplasmas for nanomaterials synthesis *J. Phys. D: Appl. Phys.* **43** 323001

[3] Chan C K, Peng H L, Liu G, McIlwrath K, Zhang X F, Huggins R A and Cui Y 2008 High-performance lithium battery anodes using silicon nanowires *Nat. Nanotechnol.* **3** 31–35

[4] Magasinski A, Dixon P, Hertzberg B, Kvit A, Ayala J and Yushin G 2010 High-performance lithium-ion anodes using a hierarchical bottom-up approach *Nat. Mater.* **9** 353–8

[5] Yan Z and Guo J 2019 High-performance silicon-carbon anode material via aerosol spray drying and magnesiothermic reduction *Nano Energy* **63** 103845

[6] Nava G, Schwan J, Boebinger M G, McDowell M T and Mangolini L 2019 Silicon-core–carbon-shell nanoparticles for lithium-ion batteries: rational comparison between amorphous and graphitic carbon coatings *Nano Lett.* **19** 7236–45

[7] Schwan J, Nava G and Mangolini L 2020 Critical barriers to the large scale commercialization of silicon-containing batteries *Nanoscale Adv.* **2** 4368–89

[8] Liu X H, Zhong L, Huang S, Mao S X, Zhu T and Huang J Y 2012 Size-dependent fracture of silicon nanoparticles during lithiation *ACS Nano* **6** 1522–31

[9] Husmann E, Thimsen E and Chen X 2021 Particle charge distributions in the effluent of a flow-through atmospheric pressure low temperature plasma *Plasma Sources Sci. Technol.* **30** 075030

[10] Chen X and Hogan C J 2021 Nanoparticle dynamics in the spatial afterglows of nonthermal plasma synthesis reactors *Chem. Eng. J.* **411** 128383

[11] Alexandrov A L, Schweigert I V and Ariskin D A 2013 Kinetic simulations of argon dusty plasma afterglow including metastable atom kinetics *J. Exp. Theor. Phys.* **116** 663–72

[12] Couëdel L, Samarian A A, Mikikian M and Boufendi L 2008 Influence of the ambipolar-to-free diffusion transition on dust particle charge in a complex plasma afterglow *Phys. Plasmas* **15** 063705

[13] Denysenko I B, Azarenkov N A, Ostrikov K and Yu M Y 2018 Electron energy probability function in the temporal afterglow of a dusty plasma *Phys. Plasmas* **25** 013703

[14] Denysenko I B, Stefanović I, Azarenkov N A and Burmaka G P 2015 Effect of secondary emission on the argon plasma afterglow with large dust density *Phys. Plasmas* **22** 023702

[15] Denysenko I, Stefanović I, Sikimić B, Winter J, Azarenkov N A and Sadeghi N 2011 A global model for the afterglow of pure argon and of argon with negatively charged dust particles *J. Phys. D: Appl. Phys.* **44** 205204

[16] Ilija S, Nader S and Jörg W 2010 The influence of C_2H_2 and dust formation on the time dependence of metastable argon density in pulsed plasmas *J. Phys. D: Appl. Phys.* **43** 152003

[17] Lopez T and Mangolini L 2014 On the nucleation and crystallization of nanoparticles in continuous-flow nonthermal plasma reactors *J. Vac. Sci. Technol.* B **32** 061802

[18] Henriksen G L, Amine K and Liu J 2003 *Materials Cost Evaluation Report for High-Power Li-Ion Batteries* (United States: Department of Energy—Office of Scientific and Technical Information)

[19] Vemury S, Janzen C and Pratsinis S E 1997 Coagulation of symmetric and asymmetric bipolar aerosols *J. Aerosol. Sci.* **28** 599–611

[20] Kortshagen U and Bhandarkar U 1999 Modeling of particulate coagulation in low pressure plasmas *Phys. Rev.* E **60** 887–98

[21] Allen J E 1992 Probe theory—the orbital motion approach *Phys. Scr.* **45** 497–503

[22] Mott-Smith H M and Langmuir I 1926 The theory of collectors in gaseous discharges *Phys. Rev.* **28** 727–63

[23] Allen J E, Annaratone B M and de Angelis U 2000 On the orbital motion limited theory for a small body at floating potential in a Maxwellian plasma *J. Plasma Phys.* **63** 299–309

[24] Gatti M and Kortshagen U 2008 Analytical model of particle charging in plasmas over a wide range of collisionality *Phys. Rev.* E **78** 046402 1–6

[25] McAfee K B, Sipler D and Edelson D 1967 Mobilities and reactions of ions in argon *Phys. Rev.* **160** 130–5

[26] Bogaerts A and Gijbels R 2000 Effects of adding hydrogen to an argon glow discharge: overview of relevant processes and some qualitative explanations *J. Anal. At. Spectrom.* **15** 441–9

[27] Videnović I R, Konjević N and Kuraica M M 1996 Spectroscopic investigations of a cathode fall region of the Grimm-type glow discharge *Spectrochim. Acta* B **51** 1707–31

[28] Mangolini L and Kortshagen U 2009 Selective nanoparticle heating: another form of nonequilibrium in dusty plasmas *Phys. Rev.* E **79** 026405

[29] Gerber R A and Gerardo J B 1973 Ambipolar-to-free diffusion: the temporal behavior of the electrons and ions *Phys. Rev.* A **7** 781–90

[30] Liebermann M and Lichtenberg A J 2005 *Principles of Plasma Discharges and Materials Processing* (New York: WIley)

[31] Stefanović I, Berndt J, Marić D, Šamara V, Radmilović-Radjenović M, Petrović Z L, Kovačević E and Winter J 2006 Secondary electron emission of carbonaceous dust particles *Phys. Rev.* E **74** 026406

[32] Woodard A, Shojaei K, Berrospe-Rodriguez C, Nava G and Mangolini L 2020 Electron emission from particles strongly affects the electron energy distribution in dusty plasmas *J. Vac. Sci. Technol.* A **38** 023005

[33] Le Picard R and Girshick S L 2016 The effect of single-particle charge limits on charge distributions in dusty plasmas *J. Phys. D: Appl. Phys.* **49** 095201

[34] Bronold F X, Deutsch H and Fehske H 2009 Physisorption kinetics of electrons at plasma boundaries *Eur. Phys. J.* D **54** 519–44

[35] Hogan Jr C J and de la Mora J F 2009 Tandem ion mobility-mass spectrometry (IMS-MS) study of ion evaporation from ionic liquid-acetonitrile nanodrops *Phys. Chem. Chem. Phys.* **11** 8079–90

[36] Kramer N J, Anthony R J, Mamunuru M, Aydil E S and Kortshagen U R 2014 Plasma-induced crystallization of silicon nanoparticles *J. Phys. D: Appl. Phys.* **47** 075202

[37] Hawa T and Zachariah M R 2005 Coalescence kinetics of bare and hydrogen-coated silicon nanoparticles: a molecular dynamics study *Phys. Rev.* B **71** 165434

[38] Zachariah M R and Carrier M J 1999 Molecular dynamics computation of gas-phase nanoparticle sintering: a comparison with phenomenological models *J. Aerosol Sci.* **30** 1139–51

[39] Friedlander S K and Wu M K 1994 Linear rate law for the decay of the excess surface area of a coalescing solid particle *Phys. Rev.* B **49** 3622–4